ELSEVIER

Enhanced resolution for EPR imaging by two-step deblurring

Rizwan Ahmad [a,b], Bradley Clymer [a,c], Deepti S. Vikram [b], Yuanmu Deng [b],
Hiroshi Hirata [d], Jay L. Zweier [b], Periannan Kuppusamy [b,*]

[a] *Department of Electrical and Computer Engineering, The Ohio State University, College of Engineering, Columbus, OH 43210, USA*
[b] *Center for Biomedical EPR Spectroscopy and Imaging, Davis Heart and Lung Research Institute, Department of Internal Medicine,
The Ohio State University, College of Medicine, Columbus, OH 43210, USA*
[c] *Department of Biomedical Engineering, The Ohio State University, College of Engineering, Columbus, OH 43210, USA*
[d] *Department of Electrical Engineering, Yamagata University, Yonezawa, Yamagata, 992-8510, Japan*

Abstract

The broad spectrum of spin probes used for electron paramagnetic resonance imaging (EPRI) result in poor spatial resolution of the reconstructed images. Conventional deconvolution procedures can enhance the resolution to some extent but obtaining high resolution EPR images is still a challenge. In this work, we have implemented and analyzed the performance of a postacquisition deblurring technique to enhance the spatial resolution of the EPR images. The technique consists of two steps; noniterative deconvolution followed by iterative deconvolution of the acquired projections which are then projected back using filtered backprojection (FBP) to reconstruct a high resolution image. Further, we have proposed an analogous technique for iterative reconstruction algorithms such as multiplicative simultaneous iterative reconstruction technique (MSIRT) which can be a method of choice for many applications. The performance of the suggested deblurring approach is evaluated using computer simulations and EPRI experiments. Results suggest that the proposed procedure is superior to the standard FBP and standard iterative reconstruction algorithms in terms of mean-square-error (MSE), spatial resolution, and visual judgment. Although the procedure is described for 2D imaging, it can be readily extended to 3D imaging.
© 2006 Elsevier Inc. All rights reserved.

Keywords: EPR imaging; Deconvolution; Filtered backprojection; Iterative reconstruction technique

1. Introduction

Electron paramagnetic resonance imaging (EPRI) is a noninvasive technique that is capable of mapping the distribution of unpaired electrons [1,2]. It has a distinct advantage in many medical applications [3–5] where it can be used for the direct measurement of both endogenous and introduced free radicals. In the past few years, the potential applications of EPRI to studies of living biological systems have been recognized [6–9]. Despite all the progress made in the last two decades, the acquisition of high quality images of biological samples has been limited by

several technical factors including resolution, sensitivity, and speed of data acquisition [10,11].

Although spatial EPRI is capable of mapping the distribution of free radicals, the broad absorption spectra of EPR along with low signal-to-noise (SNR) make it particularly difficult to generate images with high spatial resolution which can be crucial in extracting fine details of the distribution of free radicals. In EPRI, the spatial resolution depends on a number of factors such as the intrinsic linewidth of the paramagnetic species which is generally three orders of magnitude larger than that of NMR, gradient strength, SNR, and the effectiveness of the deconvolution procedure. The resolution can be enhanced by using probes with narrow spectrum and by applying high gradient strengths. On the other hand, increasing the gradient strength lowers the SNR. Hence, increasing the gradient

strength beyond a certain limit may result in degradation of the image quality because of inadequate SNR. Therefore, a postprocessing procedure to enhance the image resolution would be useful.

It should be noted that this work is limited to purely spatial EPRI where spectral shape is considered to be invariant throughout the object. Thus, for samples having spatially varying spectral shapes or multiple radical species, purely spatial EPRI is incapable of generating unambiguous distribution of the free radicals. In order to solve this problem an additional dimension, the spectral dimension, is required in the EPRI to hold the spectral shape information. The imaging technique that also includes a spectral dimension is termed as spectral–spatial imaging. Although, acquiring the spectral dimension eliminates the necessity to perform deconvolution, it increases the data acquisition time considerably. Therefore, for objects with spatially invariant spectral shape, a more attractive solution is to perform purely spatial EPRI and rely on a deconvolution procedure to obtain high resolution images.

In EPRI, conventional noniterative deconvolution is generally applied to suppress the effects of system blurring and hence to improve the spatial resolution of the image. The deconvolution, however, tends to amplify the high frequency component of the measured projection data, which is primarily noise. Therefore, lowpass filtering is generally applied to each projection to suppress the high frequency components and to avoid the division-by-zero problem. This lowpass filtering, at the same time, introduces undesired blurring in the projections and consequently in the reconstructed image. In this work, we present a deblurring technique to enhance the spatial resolution beyond the limits of the conventional deconvolution. The technique is based on the concept of iterative deconvolution [12] which has been effective in generating superresolution images in many other fields including MRI. In this paper, however, the deblurring procedure is actually carried out in two steps [13], i.e., the conventional noniterative deconvolution followed by the iterative deconvolution to suppress the blurring introduced by the lowpass filtering of the noniterative deconvolution of the first step.

The implementation of the suggested deblurring approach is described for two reconstruction methods, i.e., filtered backprojection (FBP) and iterative reconstruction schemes. For FBP, all the projections are deconvolved using the previously proposed [13] two-step deblurring procedure before applying back projection. For the iterative reconstruction [14–16], we have proposed an analogous two-step deblurring procedure in which the first step is the same, i.e., each projection is deconvolved by the conventional noniterative procedure, but the second step (iterative deconvolution), to suppress the blurring introduced by the lowpass filtering in the first step, is not performed explicitly but is rather merged with the iterative reconstruction procedure itself. The iterative reconstruction algorithm used in this research is multiplicative simultaneous iterative reconstruction technique (MSIRT) [17], and we

expect similar results for the other iterative reconstruction techniques. The simulation and EPRI experimental results suggest that the proposed deblurring scheme generates images with substantial improvement in the reconstruction quality for both the FBP and the MSIRT for a variety of imaging parameters including different SNR and gradient strengths. The figures of merit to evaluate the performance of the suggested deblurring technique are mean-square-error (MSE) and the spatial resolution which is measured in terms of the feature-preserving capabilities of the reconstruction.

2. Theory

2.1. Data acquisition

Most of the EPR experiments are conducted in continuous wave (CW) domain as the technical challenges associated with pulsed EPR [18] limit its broad use. In CW EPRI, the data are acquired in the form of projections [19] which are the absorption signal detected by sweeping the main magnetic field in the presence of a linear static magnetic field gradient. The orientation of the acquired projection is determined by the direction of the magnetic field gradient which is a vector sum of three independent and mutually orthogonal field gradients. A projection of a 2D object $f(x_1, x_2)$ along orientation θ is defined as

$$y(r) = \int_{-\infty}^{\infty} \int_{-\infty}^{\infty} f(x_1, x_2)\delta(x_1\cos\theta + x_2\sin\theta - r)\mathrm{d}x_1\,\mathrm{d}x_2 \tag{1}$$

where r is the spatial coordinate. The measured projection, however, is the convolution of the true spatial profile of the paramagnetic material $y(r)$ and the transfer function which, for EPRI, is modeled from spectral shape function, $p_0(r)$, which is the absorption signal measured in the absence of magnetic field gradient.

$$p(r) = y(r) \otimes p_0(r) \tag{2}$$

where $\otimes$ represents convolution. In Fourier domain

$$P(k) = Y(k)P_0(k) \tag{3}$$

where $P(k)$, $Y(k)$, and $P_0(k)$ are the 1D Fourier transforms of $p(r)$, $y(r)$, and $p_0(r)$, respectively.

It should be noted that Eq. (2) is only valid when $p_0(r)$ is spatially invariant throughout the object. However, this assumption may not precisely hold for situations where the experimental conditions such as variations in the RF phase, the B1 amplitude, or the heterogeneous physiological properties of the in vivo sample may cause $p_0(r)$ to vary with space. In this case, reconstruction results based on most deconvolution procedures including the one proposed in this work would be prone to ambiguities.

The spectral shape function $p_0(r)$ depends on the paramagnetic species under study, and usually belongs to a parametric family of functions such as Lorentzian, Gaussian, or Voigt [20]. The width of $p_0(r)$, also known as line-

width, directly affects the image resolution. A spectrum with large linewidth results in excessive smearing or blurring of the projection data and hence generates images with poor spatial resolution. The effect of image blurring can be reversed by deconvolving each projection, which is usually carried out in the Fourier domain.

$$Y(k) = \frac{P(k)}{P_0(k)} \qquad (4)$$

In the presence of noise, however, the division by $P_0(k)$ results in noise amplification and division-by-zero problems. Therefore, it is a common practice to apply a lowpass windowing function before dividing by $P_0(k)$.

$$Y_w(k) = \frac{[P(k)W(k)]}{P_0(k)} \qquad (5)$$

Multiplication by the lowpass function $W(k)$ introduces blurring in the projections and consequently in the reconstructed image. A selection of an excessively broad $W(k)$ results in a noisier reconstruction while a selection of an excessively narrow $W(k)$ results in blurred images. Optimum choices of the window function and its cutoff frequency k_c are usually content dependant. A few systematic approaches to determine the cutoff frequency of $W(k)$ have been proposed [21].

In the remainder of the paper, for brevity, we drop the variables r and k. Lower-case represents a variable in the image domain while upper-case represents a variable in the Fourier domain.

2.2. Two-step deblurring

Iterative constrained deconvolution has been applied effectively for solving the deblurring problem in image reconstruction such as in optical imaging [22] and MRI [23]. For the iterative deconvolution, the initial estimate y^0 of the true spatial profile is convolved with a known transfer function to generate an output which is compared with the measured data (i.e., projections) and the difference is fed back to update the estimate. The process is repeated until the update is below some threshold value or some other criterion is reached. There are several iterative deconvolution techniques available [24], each of them differing in the way the correction term is calculated and the update is applied. The Jansson–van Citteret [25] type algorithm that is used in this work is a commonly used example of the iterative deconvolution. It should be noted that any constraint based on a priori information (such as non-negativity) can be embedded in the iterative deconvolution procedure to improve the performance. Unfortunately, the van Citteret [12] or similar iterative deconvolution techniques have the tendency to generate noisy solutions [26] which may not be useable without further processing (pre- or postfiltering of the data). The recently proposed two-step deblurring procedure, on the other hand, has been shown to be effective in deblurring individual projections without noise amplification. Although, the previous work does not

involve image reconstruction, it describes the two-step technique to deblur acquired 1D projections. In this work, we have shown that the two-step deblurring applied either explicitly or by embedding it within the reconstruction technique results in enhanced spatial resolution of the reconstructed image. The complete procedure for two-step deblurring is described in Fig. 1. First, an acquired projection p is deconvolved noniteratively and later the output y_w is further deconvolved using the iterative scheme. The point spread function w used in the iterative scheme is the inverse Fourier transform (IFT) of the lowpass window function W used in noniterative deconvolution. In Fig. 1, μ is the relaxation factor [27] that controls the gain of the feedback loop.

As is the case with the conventional deconvolution, the cutoff frequency k_c of W affects the reconstruction quality of the two-step deblurring approach. It has been suggested [13] that the combination of a smaller k_c values followed by iterative deconvolution generates better results than using a larger k_c values. In this work, W is selected to be a Hamming window with its k_c chosen empirically for each combination of imaging parameters such that the best results in term of feature identification, which is one of the figures of merit, were obtained. A more systematic way to select the window type and its cutoff frequency k_c requires further investigation.

2.3. Iterative reconstruction

The FBP, which is based on direct inversion of the Radon transform [28], is the most commonly used reconstruction technique from the projection data. For a large
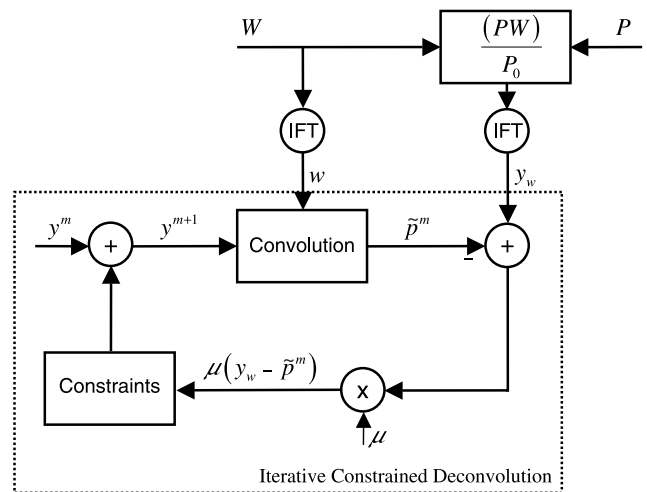

Fig. 1. Flow chart of two-step deblurring. Inside the dotted box is a commonly used iterative deconvolution technique. Here, W is the lowpass window function in the Fourier domain, P is the measured projection data in the Fourier domain, y_w is partially deconvolved projection data, point spread function w, which is an IFT of W, is used to iteratively deconvolve y_w, $\tilde{p}^m$ is partially deconvolved projection data estimate after mth iteration, y^m is the deconvolved projection data (spatial profile) estimate after mth iteration, and μ is the relaxation factor.

number of projections, the FBP generate images with reasonable quality. In EPRI, there are usually a limited number of projections available since data acquisition is a time consuming process. Hence, for many applications the FBP may not generate desirable results since the reconstruction exhibits severe streak-artifacts for a small number of projections, which may degrade the image quality to an unacceptable level. In addition, the FBP does not incorporate the measurement noise and the transfer function of the system. As a result, the acquired data have to be deconvolved separately before applying the FBP. To address these issues, there are several iterative reconstruction algorithms [29,30] available such as additive algebraic reconstruction technique (AART), multiplicative algebraic reconstruction technique (MART), and multiplicative simultaneous iterative reconstruction technique (MSIRT). These different approaches to the iterative reconstruction differ from one another in the way the correction term is derived and the update to the new estimate is applied. Recently, reconstructions based on the iterative schemes have been presented for EPRI [31,32].

The transfer function modeled from the observed spectral shape can be incorporated in the iterative reconstruction by computing the correction term (to update the image estimate) based on the dissimilarity (e.g., difference or ratio) between the measured projections and the convolution of spatial profile estimate with the transfer function. If the spectral shape corresponds to a parametric family of functions, the observed spectral shape can be curve-fitted by an appropriate function to generate a noise-free transfer function for improved results. In this work, the observed spectral shape p_0 was taken as the transfer function and no curve fitting was applied.

The results presented in this work are based on the MSIRT. Although, we observed comparable performance for the AART and MART, the MSIRT exhibited a slightly better performance at low SNR which is usually the case for EPRI. A detailed comparison of various iterative reconstruction techniques for EPRI is left for further studies. An iteration of MSIRT [17], after taking into account the transfer function, is given by

$$f_j^{m+1} = f_j^m \underbrace{\frac{\sum_{i=1}^{I} \frac{p_i c_{ij}}{\sum_{j=1}^{J} c_{ij}}}{\sum_{i=1}^{I} \frac{p_i^m c_{ij}}{\sum_{j=1}^{J} c_{ij}}}}_{\text{Correction}} \qquad (6)$$

where

$$p_i^m = y_i^m \otimes p_0 \qquad (7)$$

where j is the pixel index, J is total number of pixels, m is the iteration number, i is the projection index, I is the total number of projections, p_i is the ith measured projection, y_i^m is the estimate of ith deblurred projection calculated by the Radon transform of updated image estimate f^{m+1}, and weight function c_{ij} represents the path length of ray i that lies in cell j [30].

On the down side, the time required for one iteration of the iterative reconstruction is approximately 2–3 times more than that of the FBP, and depending on the algorithm settings and convergence criterion, 10–100 iterations are used for one reconstruction [16]. To address this issue, a few algorithms have been proposed [33,34] to speed up the reconstruction process of the iterative schemes. Moreover, increase in computation power (due to the availability of faster microprocessors and memory) has reduced the reconstruction time even further. As a result, these iterative reconstructions schemes are emerging as an attractive alternative to the FBP. We observed that the total time for 2D MSIRT reconstruction in Matlab (Natick, MA) from 36 projections (each with a length of 275 data points) for 100 iterations was about 80 s.

One major disadvantage of the iterative schemes is that the reconstruction shows excessive statistical noise if the projection data are noisy which may result in degradation of the spatial resolution. In EPRI, where SNR is generally low, a direct use of iterative reconstruction schemes may not generate desired results. Different techniques to solve this problem have been investigated for other applications. One possible solution is to regularize the reconstruction which can be achieved by restricting the reconstruction to be composed of functions that possess some smoothing properties [35]. A second solution is to limit the number of iterations [36] and stop the reconstruction process before the noise deterioration degrades the image quality. A third solution is to postprocess the reconstructed image to suppress the noise. In clinical applications, the postprocessing method is generally applied because of its flexibility and fast speed. Although, postfiltering the reconstructed image effectively suppresses the noise, it may also degrade the spatial resolution. The results presented in this paper indicate that the suggested deblurring technique has the potential to generate smooth images with high spatial resolution that, in many cases, cannot be achieved by postfiltering.

2.4. Implementation of two-step deblurring for FBP and MSIRT

As mentioned earlier, the FBP and iterative reconstruction schemes have their advantages and disadvantages, and depending on the application one may be more suited than the other. A detailed comparison of the FBP and the iterative reconstruction schemes is beyond the scope of this research. In this work, we have provided two variations of the two-step deblurring approach; one for the FBP and other for the iterative reconstruction schemes. For the FBP, each projection is deconvolved using the previously proposed idea of two-step deblurring approach shown in Fig. 1. The deconvolved projections are then filtered using a highpass ramp filter before applying back projection. We abbreviate this procedure (two-step deblurring followed by the FBP) as FBP$_m$ to distinguish it from the conventional FBP.

For the iterative reconstruction, the two-step deblurring procedure is shown in Fig. 2. All the projections are partially deconvolved using Eq. (5) to generate y_w before applying the MSIRT. Here, the second step (iterative deconvolution) is not applied explicitly and is effectively integrated into the MSIRT. We abbreviate this procedure as MSIRT$_m$ to distinguish it from the conventional MSIRT described in Eq. (6). While the MSIRT operates directly on the acquired noisy projections, MSIRT$_m$ operates on partially deconvolved projections with suppressed noise. Although it is possible to decouple the deconvolution from iterative reconstruction by performing the two-step deblurring prior to the iterative reconstruction, we observed an improvement in the reconstruction quality by incorporating the second step of deblurring into the MSIRT. Like other iterative deconvolution techniques, the two-step deblurring performed on individual projections has a tendency to introduce false spikes in the projections. Since the iterative reconstruction schemes including MSIRT seek an image estimate that comes as close to input data as possible, the spikes in the input data (deconvolved projections) may generate pronounced artifacts in the reconstructed image. On the other hand, partially deconvolved projections are smoother for which the MSIRT generates results devoid of artifacts with clear background. The first step of partial deconvolution of the projections effectively suppresses noise due to the lowpass nature of w, but at the same time it also introduces blurring in the projections. The further deblurring of y_w is accomplished by convolving the spatial profile estimate y^m with w and feeding the dissimilarity between $y^m \otimes w$ and y_w (e.g., the difference or the ratio) back to the image estimate. Since y_w is an approximation of $y^m \otimes w$, reducing the dissimilarity between $y^m \otimes w$ and y_w drives y^m towards y. In Fig. 2, [·]

represents an operator to calculate the correction term to update the image estimate in each iteration. For conventional MSIRT, the correction term is given in Eq. (6) while for MSIRT$_m$ the correction term is given in Eq. (8).

$$f_j^{m+1} = f_j^m \underbrace{\frac{\sum_{i=1}^{I} \frac{y_{wi} c_{ij}}{\sum_{j=1}^{J} c_{ij}}}{\sum_{i=1}^{I} \frac{\tilde{p}_i^m c_{ij}}{\sum_{j=1}^{J} c_{ij}}}}_{\text{Correction}} \qquad (8)$$

where

$$\tilde{p}_i^m = y_i^m \otimes w \qquad (9)$$

Although, we observed similar results with Gaussian and Hanning windows, we have used a Hamming window for W since its use for the deconvolution of EPR projection data has already been reported [21].

2.5. Figure of merit

The commonly used mean-square-error (MSE) is used as a quantitative measure of the image quality. The MSE is defined as the average of the squared difference between the reference image (ground truth) and the reconstructed image.

The quantification of the spatial resolution for 1D objects is well established. Generally, the spatial resolution for a 1D object is measured as either the edge preserving capability or the least spatial distance between two distinct features that can be successfully separated from one another for some threshold. For an object with more than one spatial dimension, separation of a feature, and hence the direct quantification of the spatial resolution, is more involved since the feature separation from its surroundings
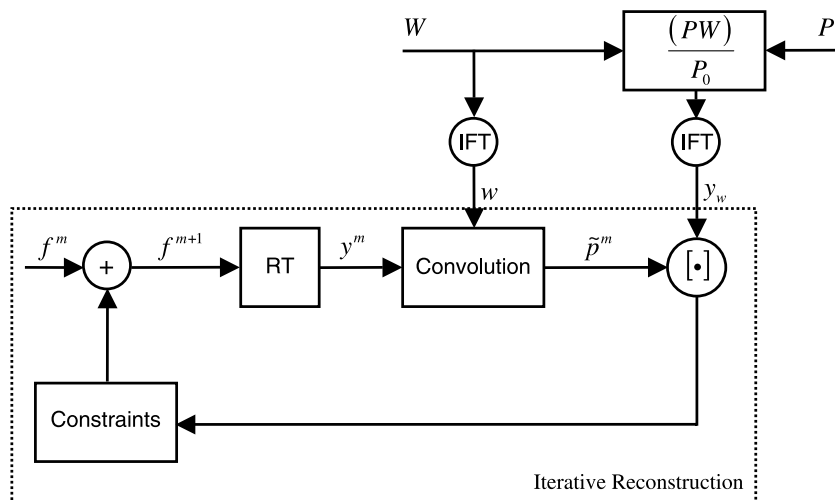

Fig. 2. Flow chart of the iterative reconstruction merged with the two-step deblurring. Inside the dotted box is a prototype for an iterative reconstruction technique where [·] is the operator to calculate the correction term to update the estimate. Here, W is the lowpass window function in the Fourier domain, P is the measured projection data in the Fourier domain, y_w is partially deconvolved projection data after noniterative deconvolution, point spread function w, which is an IFT of W, is used to iteratively deconvolve y_w, $\tilde{p}^m$ is the estimate of partially deconvolved projection data after mth iteration, y^m is the estimate of the deconvolved projection data (spatial profile) after the mth iteration, f^m is the object estimate after the mth iteration, and RT represents Radon transform.

is required to examined in all orientations. Moreover, due to the structured artifacts in the EPRI reconstruction, the reconstructed image may possess different resolutions in different orientations depending on the choice of projection set. On the other hand, the capability to identify closely placed features in an image is an effective way to judge the over all spatial resolution. We have used a three step procedure to judge if a feature present in the reference image can actually be identified in the reconstructed image. First, edge detection is performed using Laplacian of Gaussian [37] (LoG) with a 2D isotropic Gaussian kernel having a standard deviation of two pixels. Second, a morphological filter [38] is used to fill all the close contours generated by the edge detector. Third, segmentation is carried out by assigning all the connected pixels to one entity. Now the segmented image is compared with the reference image. If a feature in the segmented image matches the corresponding feature in the reference image, it is counted as identified. Although there are number of configuration parameters related to a feature, we have chosen centroid and area (with the tolerance of 25%) to match a given feature between the reconstructed and the reference images.

3. Results

3.1. Simulations

For performance evaluation, the reconstruction results from the regular FBP and MSIRT were compared with FBP_m and $MSIRT_m$ where the two-step deblurring approach was included in the reconstruction. A 192×192 digital phantom shown in Fig. 3 was used for the simulations. The phantom consisted of 15 dots arranged on an equilateral triangular grid. The piecewise continuous and a well organized pattern of the phantom makes for a more direct judgment of the reconstruction quality. The imaging parameters were chosen to simulate EPRI experiments at L-band (1.2 GHz). All simulations were performed using Matlab. The imaging parameters in the simulation were as follows: field of view, 2×2 cm^2; data points per projec-

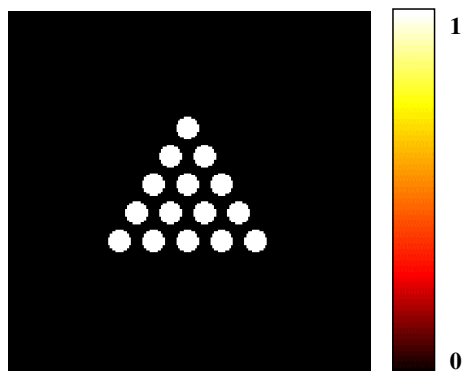Fig. 3. A 192×192 digital phantom alongside the colormap used in all the simulations. The phantom consists of fifteen dots arranged on an equilateral triangular grid.

tion, 275; width of Lorentzian spectral shape, 450 mG. A linear baseline correction was applied to each projection prior to deconvolution. The projection data were acquired for combinations of two different gradient strengths (4 G/cm and 6 G/cm), four different SNR (32, 22, 12, and 7) measured as the ratio of peak-signal amplitude to peak-noise amplitude for the first derivative of the spectral shape function recorded in the absence of magnetic field gradient, and two different number of projections ($n = 24$ and $n = 36$). The results are shown in Figs. 4 and 5 for FBP and MSIRT, respectively. After reconstruction, 32 pixels were cropped from each border of the image for better visualization. For FBP-based reconstructions, a 20% background cut was applied such that all the pixels in the reconstructed image with intensity less that the 20% of the peak value were set to zero. On the other hand, no such background cut was applied for the iterative reconstruction since the background was already devoid of reconstruction artifacts. To demonstrate the convergence behavior, the MSE vs. number of iteration curve is given in Fig. 6 for one set of imaging parameters. We observed similar convergence behavior for the other imaging parameters.

3.2. EPRI experiment

For validation of the technique, an experimental phantom shown in Fig. 7A was constructed from 15 capillary tubes glued together to form an equilateral triangle. Each capillary tube had an inner diameter of 0.9 mm and an outer diameter of 1.4 mm. All the tubes were filled to a height of 10 mm with 2 mM ^{15}N-PDT (4-oxo-2,2,6,6-tetramethyl-piperidine-d_{16}-^{15}N-oxy) radical dissolved in distilled water. The center field and sweep width were selected such that the observed signal was solely due to one (low field) of the two lines of the ^{15}N-PDT spectrum, while the other line was put safely outside the range of the magnetic field sweep. Hence, we were not required to perform a hyperfine correction. The measured room air peak-to-peak linewidth was 440 mG. Imaging was performed on an L-band (1.2 GHz) EPRI system with a volume resonator with a diameter of 12.6 mm and a useable height of 12 mm. Spectrometer settings were: incident power, 4 mW; scan time per projection, 5.24 s; field of view, 25×25 mm^2; gradient strengths, 3.5 and 6 G/cm; modulation amplitudes, 220, 120, 40, 20, 10 mG (with the corresponding measured SNR of 200, 100, 27, 16, 8). Since spectral shape varies with the modulation amplitude, a separate spectral shape was observed for each modulation amplitude. A total of 256 projections were acquired for each combination of SNR and gradient strength. Originally, each acquired projection had 1024 data points which were downsampled to 275 points for faster reconstruction. Again, linear baseline correction was applied to each projection before the deconvolution. However, no correction for B1 field inhomogeneities was applied [39]. After reconstruction, 22% of the image was cropped from each border for better visualization. The reference image shown in Fig. 7B was
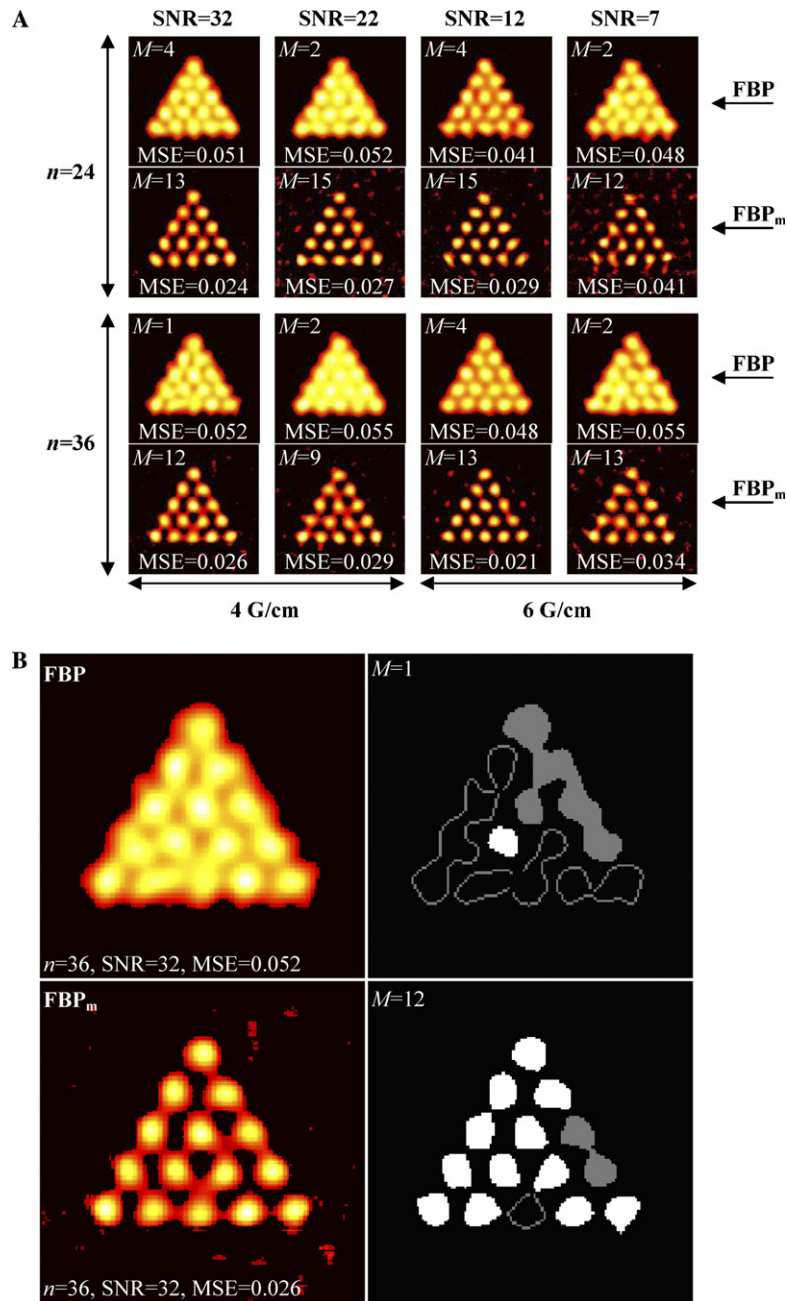
Fig. 4. Simulation results for the FBP and the FBP_m which is the two-step deblurring followed by the regular FBP. (A) Reconstruction results for various imaging parameters. Here, MSE is the mean-square-error and M is the number indicating the tubes successfully identified by the feature extraction routine. (B) Zoomed version of reconstruction results for one set of imaging parameters. The first column shows the reconstruction from FBP and FBP_m while the second column shows the corresponding segmented image. A white entity represents a successfully identified tube, a filled gray entity represents a feature that is not recognized as tube and a gray contour represents the feature in the reconstruction image for which the edge detector could not find a close contour.

reconstructed using the FBP from 256 projections acquired at the modulation amplitude of 220 mG (SNR of 200) and the gradient strength of 10 G/cm. Again, a 20% background cut was applied to all the FBP-based reconstructions including the reference image. The experimental results for the FBP and the MSIRT are shown in Figs. 8 and 9, respectively. Although the experiments were performed and the data was analyzed for all possible combinations of the stated SNR and gradient strengths, only a fraction of the data is presented in this work. The data acquired at high gradient strengths and high SNR generated high quality images for all the techniques including the conventional reconstruction techniques. On the other hand, the data acquired at low gradient strengths and low SNR was unable to generate meaningful results by any of the techniques. Therefore, the results for these two combinations of imaging parameter are not presented in this work.
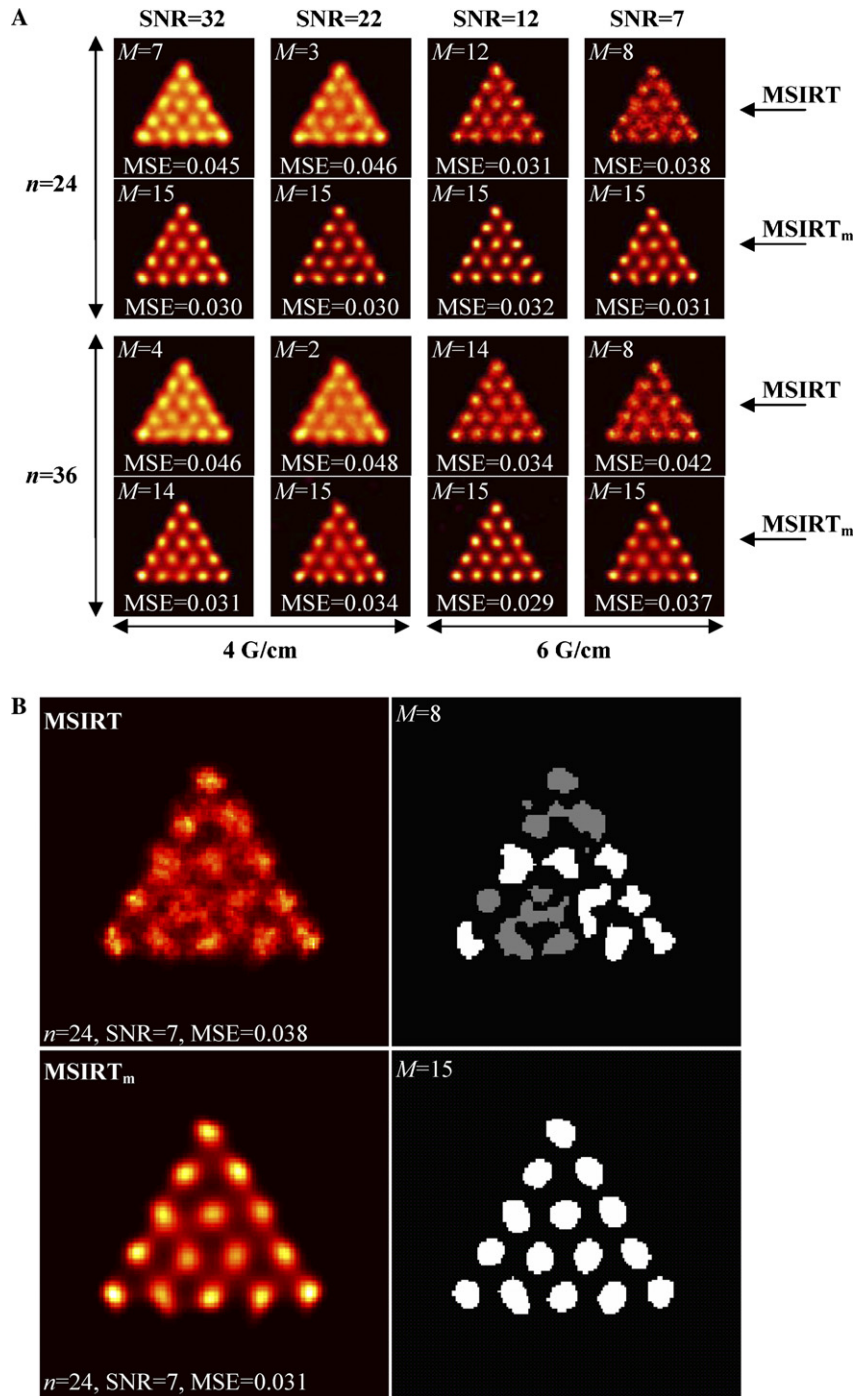
Fig. 5. Simulation results for the MSIRT and the $MSIRT_m$ which is the iterative reconstruction technique merged with two-step iterative deconvolution. (A) Reconstruction results for various imaging parameters. Here, MSE is the mean-square-error and M is the number indicating the tubes successfully identified by the feature extraction routine. (B) Zoomed version of reconstruction results for one set of imaging parameters. The first column shows the reconstruction from MSIRT and $MSIRT_m$ while the second column shows the corresponding segmented image. A white entity represents a successfully identified tube, a filled gray entity represents a feature that is not recognized as tube and a gray contour represents the feature in the reconstruction image for which the edge detector could not find a close contour.

4. Discussion

Conventional deconvolution procedures are generally applied to deblur the images to improve the spatial resolution which can be critical in identifying the details in the distribution of paramagnetic specie. The impact of decon-volution depends on the choice of the lowpass window function and its cutoff frequency. For noisy projections, increasing the cutoff frequency beyond a certain limit amplifies noise to an extent that image quality degrades to an unacceptable level. Therefore, the performance of regular noniterative deconvolution is primarily determined
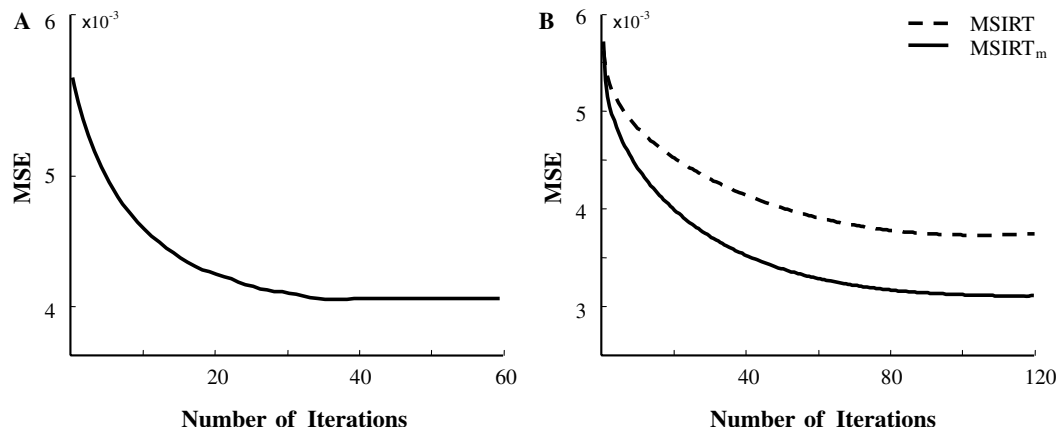
Fig. 6. Rate of convergence for one set of imaging parameters (number of projections: 24, SNR: 7, and gradient strength 6 G/cm). (A) Convergence of FBP-based reconstruction when each projection is independently deconvolved using the stated two-step deblurring approach. The MSE is calculated from the FBP-based reconstructed image after each iteration of the iterative deconvolution. (B) Convergence of MSIRT vs. $MSIRT_m$.
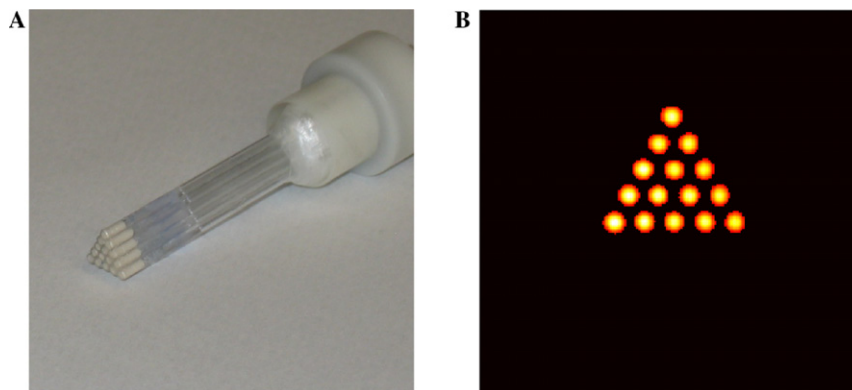

Fig. 7. Experimental phantom. (A) A phantom constructed from 15 capillary tubes arranged on an equilateral triangular grid. Each capillary tube had an inner diameter of 0.9 mm and an outer diameter of 1.4 mm. All the tubes were filled to a height of 10 mm with 2 mM concentration of ^{15}N-PDT (4-oxo-2,2,6,6-tetramethyl-piperidine-d_{16}-^{15}N-oxy) radical dissolved in distilled water. Imaging was performed using an L-band (1.2 GHz) EPRI system. (B) Reference image reconstructed using FBP from 256 projections acquired with gradient of 10 G/cm, modulation amplitude of 220 mG, and SNR of 200. Pixels with intensity less than 20% of the peak intensity were set to zero.

by the cutoff frequency whose selection is based on factors like the frequency component of the acquired projection data, convolution kernel, and the SNR. The two-step deblurring technique described in this paper generates images with resolution that cannot be achieved by the conventional methods especially for the data acquired with insufficient gradient strength (due to hardware limitations) or low SNR. The two variations of the deblurring approach, one for the FBP and the other for iterative reconstruction algorithms such as MSIRT, are presented. A total of eight datasets were considered for the simulations, each with a different combination of SNR (32, 22, 12, and 7), gradient strength (4 G/cm and 6 G/cm), and number of projections (24 and 36).

For the FBP, the simulation results displayed in Fig. 4 suggest that the image quality can be improved considerably by using the two-step deblurring procedure. The feature identification capability, in particular, is enhanced as more tubes can be successfully identified by the feature extraction routine as demonstrated in Fig. 4B. Mean fea-

ture identification capability (measured as the percentage of dots successfully identified by the routine) averaged over all the eight cases presented in Fig. 4 was increased from 17.5% to 85%. Likewise, the mean MSE averaged over all the cases was reduced from 0.050 to 0.029. It should be noted that for the FBP the suggested two-step approach does not enhance the resolution of the 2D image directly, but it rather increases the resolution of individual 1D projections. As a result, the streak artifact may also get worse as the projections get sharper. The enhanced streak artifact is especially visible for a small number of projections.

We have further extended the two-step deblurring technique for the iterative reconstruction which can be a method of choice because of its ability to generate streak-free reconstructions. Fig. 5 illustrates that the $MSIRT_m$ generates images with improved spatial resolution, considerably lower MSE, and enhanced feature identification capability. By incorporating the suggested modifications, the noise in the conventional MSIRT is greatly reduced. Quantitatively, the mean feature identification capability was increased from
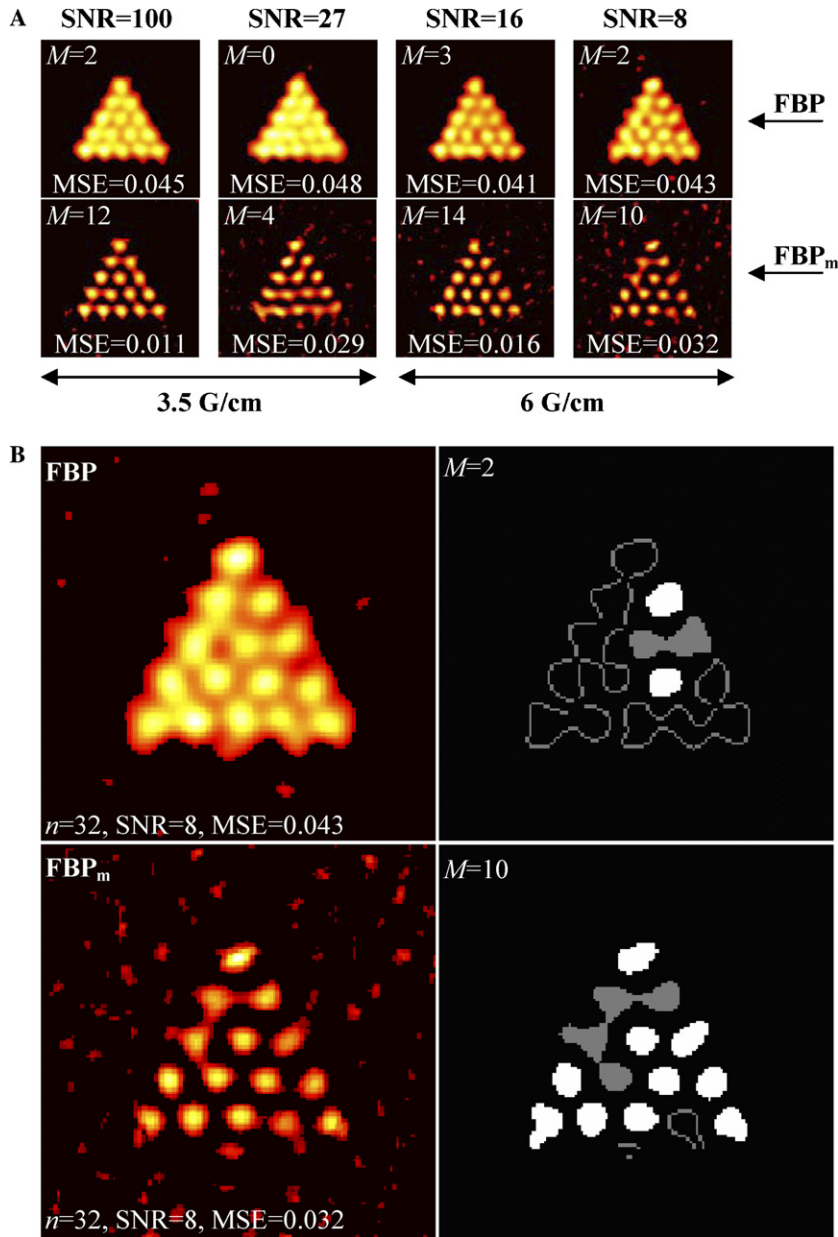
Fig. 8. Experimental results for the FBP and the FBP$_m$. (A) Reconstruction results for various imaging parameters. Here, MSE is the mean-square-error and M is the number indicating the tubes successfully identified by the feature extraction routine. (B) Zoomed version of reconstruction results for one set of imaging parameters. The first column is the reconstruction from FBP and FBP$_m$ while the second column shows the corresponding segmented image. A white entity represents a successfully identified tube, a filled gray entity represents a feature that is not recognized as tube and a gray contour represents the feature in the reconstruction image for which the edge detector could not find a close contour.

48% to 99%, while the mean MSE was reduced from 0.041 to 0.032 for all the eight cases shown in Fig. 5.

For 2D EPRI experiment, a total of four datasets were considered, each with a different combination of SNR (100, 27, 16, and 8) and gradient strength (3.5 G/cm and 6 G/cm). The results presented in Figs. 8 and 9 suggest that image quality is improved by the two-step deblurring procedure for both FBP- and MSIRT-based reconstructions. The results of 2D EPRI experiment are in accordance with the simulation results. The two-step deblurring approach generates images with lower MSE and improved feature identification capability. For FBP-based reconstructions, mean feature identification capability was increased from 12% to 67%, while the mean MSE was reduced from 0.042 to 0.022 for the four cases shown in Fig. 8. For MSIRT, mean feature identification capability was increased from 42% to 90%, and the mean MSE was reduced from 0.034 to 0.017 for the four cases presented in Fig. 9.

5. Conclusions

A two-step deblurring procedure consisting of conventional noniterative deconvolution followed by iterative deconvolution to improve the spatial resolution of the
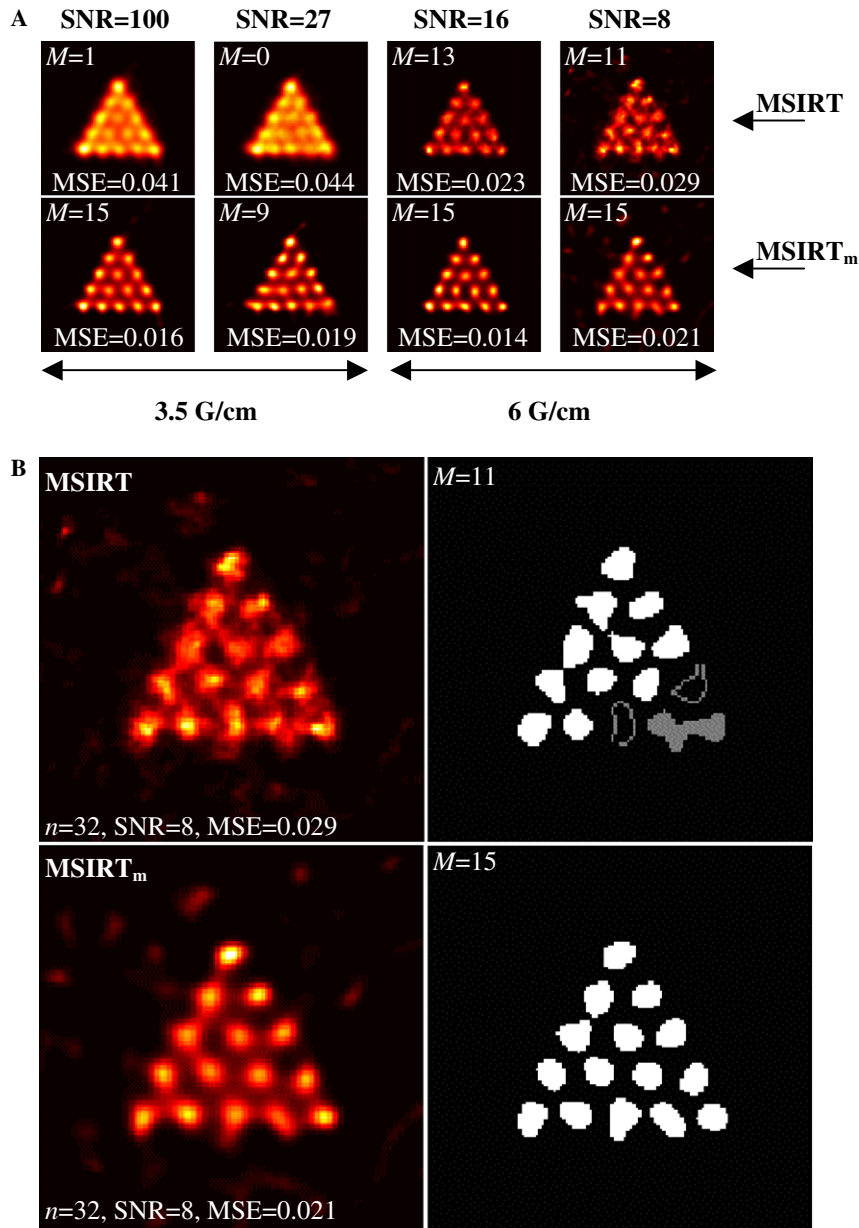
Fig. 9. Experimental results for the MSIRT and the. (A) Reconstruction results for various imaging parameters. Here, MSE is the mean square error and M is the number indicating the tubes successfully identified by the feature extraction routine. (B) Zoomed version of reconstruction results for one set of imaging parameters. The first column is the reconstruction from MSIRT and $MSIRT_m$ while the second column shows the corresponding segmented image. A white entity represents a successfully identified tube, a filled gray entity represents a feature that is not recognized as tube and a gray contour represents the feature in the reconstruction image for which the edge detector could not find a close contour.

EPR images has been proposed. The implementation is carried out for the FBP as well as for the iterative reconstruction algorithms such as MSIRT. The simulation and experimental results indicate that the inclusion of the two-step deblurring approach to FBP or MSIRT generates images which are substantially better, both qualitatively and quantitatively, to the ones based on the corresponding conventional FBP or MSIRT. The enhancement of the image quality is evident for a wide range of imaging parameters such as SNR, gradient strengths, and number of projections. Although, the procedure is explained for 2D imaging, it can be readily extended to 3D imaging.

References

[1] M. Ferrari, V. Quaresima, A. Sotgiu, Present status of electron paramagnetic resonance (EPR) spectroscopy/imaging for free radical detection, Pflugers Arch. 431 (1996) R267–R268.
[2] H. Fujii, L.J. Berliner, One- and two-dimensional EPR imaging studies on phantoms and plant specimens, Magn. Reson. Med. 2 (1985) 275–282.

[3] J. Fuchs, H.J. Freisleben, N. Groth, T. Herrling, G. Zimmer, R. Milbradt, L. Packer, One- and two-dimensional electron paramagnetic resonance imaging in skin, Free Radic. Res. Commun. 15 (1991) 245–253.

[4] A. Hochi, M. Furusawa, M. Ikeya, Applications of microwave scanning ESR microscope: human tooth with metal, Appl. Radiat. Isot. 44 (1993) 401–405.

[5] P. Kuppusamy, EPR spectroscopy in biology and medicine, Antioxid. Redox Signal 6 (2004) 583–585.

[6] P. Kuppusamy, R.A. Shankar, V.M. Roubaud, J.L. Zweier, Whole body detection and imaging of nitric oxide generation in mice following cardiopulmonary arrest: detection of intrinsic nitrosoheme complexes, Magn. Reson. Med. 45 (2001) 700–707.

[7] A. Matsumoto, S. Matsumoto, A.L. Sowers, J.W. Koscielniak, N.J. Trigg, P. Kuppusamy, J.B. Mitchell, S. Subramanian, M.C. Krishna, K. Matsumoto, Absolute oxygen tension (pO(2)) in murine fatty and muscle tissue as determined by EPR, Magn. Reson. Med. 54 (2005) 1530–1535.

[8] E.L. Rolett, A. Azzawi, K.J. Liu, M.N. Yongbi, H.M. Swartz, J.F. Dunn, Critical oxygen tension in rat brain: a combined (31)P-NMR and EPR oximetry study, Am. J. Physiol. Regul. Integr. Comp. Physiol. 279 (2000) R9–R16.

[9] M. Velayutham, H. Li, P. Kuppusamy, J.L. Zweier, Mapping ischemic risk region and necrosis in the isolated heart using EPR imaging, Magn. Reson. Med. 49 (2003) 1181–1187.

[10] Y. Deng, G. He, S. Petryakov, P. Kuppusamy, J.L. Zweier, Fast EPR imaging at 300 MHz using spinning magnetic field gradients, J. Magn. Reson. 168 (2004) 220–227.

[11] J.P. Joshi, J.R. Ballard, G.A. Rinard, R.W. Quine, S.S. Eaton, G.R. Eaton, Rapid-scan EPR with triangular scans and Fourier deconvolution to recover the slow-scan spectrum, J. Magn. Reson. 175 (2005) 44–51.

[12] P.H. van Cittert, Zum einfluss der spaltbreite auf die intensitatsverteilung der spektrallinien, Z. Phys. 69 (1931) 298–304.

[13] H. Hirata, M. Wakana, H. Susaki, Feasibility study of superresolution continuous-wave electron paramagnetic resonance imaging, Appl. Phys. Lett. 88 (2006) 254103.

[14] A.H. Andersen, Algebraic reconstruction in CT from limited views, IEEE Trans. Med. Imaging 8 (1989) 50–55.

[15] W. Richardson, Bayesian-based iterative method of image restoration, J. Opt. Soc. Am. 62 (1972) 55–59.

[16] S. Vandenberghe, Y. D'Asseler, R. Van de Walle, T. Kauppinen, M. Koole, L. Bouwens, K. Van Laere, I. Lemahieu, R.A. Dierckx, Iterative reconstruction algorithms in nuclear medicine, Comput. Med. Imaging Graph. 25 (2001) 105–111.

[17] N. Haruta, K. Ogawa, Evaluation of iterative methods for aperture correction in SPECT, Syst. Comput. Jpn. 36 (2005) 52–61.

[18] J. Bourg, M.C. Krishna, J.B. Mitchell, R.G. Tschudin, T.J. Pohida, W.S. Friauf, P.D. Smith, J. Metcalfe, F. Harrington, S. Subramanian, Radiofrequency FT EPR spectroscopy and imaging, J. Magn. Reson. B 102 (1993) 112–115.

[19] S.R. Deans, The Radon Transform and Some of its Applications, Wiley, New York, 1983.

[20] B.L. Bales, M. Peric, M.T. Lamy-Freund, Contributions to the Gaussian line broadening of the proxyl spin probe EPR spectrum due to magnetic-field modulation and unresolved proton hyperfine structure, J. Magn. Reson. 132 (1998) 279–286.

[21] H. Hirata, T. Itoh, K. Hosokawa, Y. Deng, H. Susaki, Systematic approach to cutoff frequency selection in continuous-wave electron paramagnetic resonance imaging, J. Magn. Reson. 175 (2005) 177–184.

[22] Z. Zalevsky, D. Mendlovic, Optical Superresolution, Springer, New York, 2004.

[23] H. Greenspan, G. Oz, N. Kiryati, S. Peled, MRI inter-slice reconstruction using super-resolution, Magn. Reson. Imaging 20 (2002) 437–446.

[24] J.L. Starck, E. Pantin, F. Murtagh, Deconvolution in astronomy: a review, Astron. Soc. Pac. 114 (2002) 1051–1069.

[25] P.A. Jansson, R.H. Hunt, E.K. Pyler, Resolution enhancement of spectra, J. Opt. Soc. Am. 60 (1970) 596–599.

[26] P.A. Jansson, Method of determining the response function of a high-resolution infrared spectrometer, J. Opt. Soc. Am. 60 (1970) 184–191.

[27] S. Kawata, Y. Ichioka, Iterative image restoration for linearly degraded images, J. Opt. Soc. Am. 70 (1980) 762–768.

[28] J. Radon, Uber die bestimmung von funktionen durch ihre integralwerte langs gewisser mannigfaltigkeiten, Ber. Saechsis. Akad. Wissensch. 69 (1917).

[29] J.M. Ollinger, Iterative reconstruction–reprojection and the expectation-maximization algorithm, IEEE Trans. Med. Imaging 9 (1990) 94–98.

[30] D. Mishra, J.P. Longtin, R.P. Singh, V. Prasad, Performance evalution of iterative tomography algorithms for incomplete projection data, Appl. Opt. 43 (2004) 1522–1532.

[31] Y. Chiang, P.P. Borbat, J.H. Freed, Maximum entropy: A complement to Tikhonov regularization for determination of pair distance distributions by pulsed ESR, J. Magn. Reson. 177 (2005) 184–196.

[32] J.A. Cook, N. Devasahayam, J.B. Mitchell, S. Subramanian, M.C. Krishna, Maximum entropy reconstruction methods in electron paramagnetic resonance imaging, Ann. Oper. Res. 119 (2003) 101–118.

[33] Y. Censor, J. Segman, On block-iterative entropy maximization, J. Inform. Optim. Sci. 8 (1987) 275–291.

[34] H.M. Hudon, R.S. Larkin, Accelerated image reconstruction using ordered subsets of projection data, IEEE Trans. Med. Imaging 13 (1994) 601–609.

[35] D.L. Snyder, M.I. Miller, The use of sieves to stabilize images produced with the EM algorithm for emission tomography, IEEE Trans. Nucl. Sci. 32 (1985) 3864–3872.

[36] E. Veklerov, J. Llacer, Stopping rule for the MLE algorithm based on statistical pypothesis testing, IEEE Trans. Med. Imaging 6 (1987) 313–319.

[37] D. Marr, E. Hildreth, Theory of edge detection, Proc. R. Soc. Lond. B 207 (1980) 187–217.

[38] P. Maragos, R.W. Schafer, Morphological filters-part I: their set-theoretic analysis and relations to linear shift invariant, IEEE Trans. ASSP 35 (1987) 1153–1169.

[39] G. He, S.P. Evalappan, H. Hirata, Y. Deng, S. Petryakov, P. Kuppusamy, J.L. Zweier, Mapping of the B1 field distribution of a surface coil resonator using EPR imaging, Magn. Reson. Med. 48 (2002) 1057–1062.